Experimental Analysis of Water and Slurry flows in Gravity-driven Helical Mineral Separators

Thomas Romeijn[ab*], Michael Behrens[b], Gavin Paul[b] and Dongbin Wei[b]

[a] Mineral Technologies, 11 Elysium Road, Carrara QLD 4211, Australia
[b] Faculty of Engineering and Information Technology, University of Technology Sydney, NSW 2007, Australia
*Phone number: +61 7 5569 1300, E-mail: Thomas.Romeijn@mineraltechnologies.com

Abstract

This paper aims to provide essential information of the water and slurry flow behaviour in a popular full-scale mineral separation spiral. Besides critical measurements of the free surfaces, the wall roughness and wall contact angle, novel measurements and assessment of the commonly encountered 'bubble line' are provided herein. The free surface shapes of three flows: water-only, chromite slurry and magnetite slurry are compared for the first time, which highlights operational spiral phenomena. The research provides insight into the mechanics behind the 'wetting-in' process by showing that this process affects the wall contact angle more than the surface roughness. The most representative roughness height of the spiral trough was found to be 138.4 μm and the wall contact angle of the spiral surface was 88.14°, measured in the water phase. The experiments showed that the free surface shape and the position and width of the bubble line in a water-only flow reached a steady state after 1.25 spiral turns. The results and findings are applicable to spirals of other makes and models and can validate future spiral fluid flow simulations.

Keywords

Spiral separator, Roughness, Contact angle, Free surface, Bubble line

1 Introduction

A gravity-driven helical mineral separator, commonly referred to as a ‘spiral’, separates a slurry, being a mixture of water and suspended mineral particles, into streams of different particle densities. A spiral is a key piece of equipment in transforming ore bodies into valuable commodities, due to its low cost and simple operating principles. A spiral consists of four main components: the central column, the helical surface known as the ‘trough’, the feed box and the product box, as shown in Figure 1. A slurry is fed into the feed box which directs it onto the trough. The slurry then flows down the trough where gravitational forces and the interaction of the slurry with the trough causes a separation of the slurry by particle density and size. The different streams are collected at the bottom of the spiral by the product box via different offtakes.

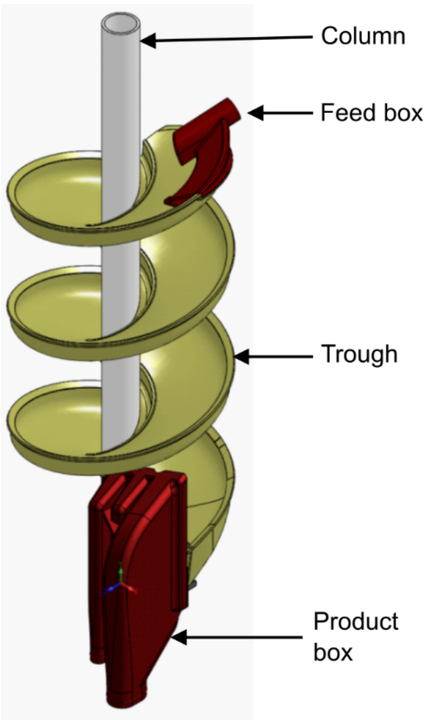

Figure 1: CS1 mineral separation spiral components

An understanding of the flow in spirals has been pursued for decades. Operational observations of the flow in spirals and measurements of their mineral separation efficiency [1-3] formed the basis of understanding the flow behaviour of spirals. These were followed by analytical approximations of the fluid behaviour in spirals [4-6]. These approximations were subsequently improved upon by increasingly complex fluid flow simulations [7-15] to enhance the understanding of the working principals of spiral separators. Due to the complex, and not completely understood [3], fluid behaviour in mineral separation spirals, Computational Fluid Dynamics (CFD) simulations have proved to be a critical tool for many research teams to advance the understanding of the governing principles at work in mineral separation spirals [7-19].

Practical CFD flow simulation requires approximation models to capture various flow effects, e.g., lift, drag and turbulence. Due to the large number of available mathematical models to approximate each of these effects, it is critical to validate the complete numerical model to confirm the appropriate selection and interaction of models. Such validation has been applied to fluid flow simulations of mineral separators by various research teams [7-19] through the comparison of the simulation outcomes with experimental data. Due to the industrial nature of a spiral, detailed experimental data available for validation have been scarce and some researchers have used scale models that approximate real spirals to validate their simulation models [13, 17, 18]. However, most research teams [7-12, 14-16, 19] validate full-scale spiral flow simulations via experimental data obtained by Holtham and Holland-Batt [4, 20-24] using a single spiral model, the Mineral Technologies' LD9. This spiral model was superseded in the early '90s [22], roughly 30 years ago. Thus, recent advances in spiral separation performance, and the possible flow alterations that underpin this, need to be re-examined. Ideally then, further improvement in the understanding of flow behaviour in full-scale spirals through CFD simulation should be based on experimental measurements on current spiral models. This paper aims to provide such data for the widespread CS1 model spiral, which is used around the world to assist in chrome beneficiation [25].

Given the complex separation processes at play in a mineral separation spiral, and the vast number of different mathematical models available in numerical simulations, it is advisable to firstly perform a CFD analysis for the simplest flow scenario, a water-only flow, to ensure that the fluid flow dynamics are fully understood and that the modelling choices are validated by experimental measurements. Such a validated water-flow simulation can then be used as the basis for the more complex CFD simulation where particles are introduced into the domain. The additional modelling choice accompanying the introduction of particles can subsequently be validated using experimental measurements of a slurry flow in a mineral separation spiral. This two-step approach has been pursued by other research teams, where a water-only flow was firstly analysed [10-12, 26] followed by a slurry flow analysis [7-9] to achieve a complete, validated CFD model that can be applied to any mineral separation spiral. To support this methodology, experimental data for both a water-only flow as well as two slurry flows through a modern separation spiral will be provided in this research article.

Particle separation arises from the interaction of the slurry with the spiral trough wall, through a radial, secondary flow in addition to a primary flow down the spiral [4, 20, 27, 28]. The difference in friction forces between the unhindered air-fluid interface and the hindered fluid-wall interface causes a secondary flow to arise [27]. Given the importance of this slurry-wall interaction on the separation behaviour, such interaction is an inevitable property of any CFD analysis.

Holland-Batt [4] performed an analytical assessment of the flow behaviour and found that for typical speeds in spirals the flow could not be described as laminar or smooth turbulent. Instead, it was found that the Manning or rough turbulent equation best described the flow behaviour in spirals. Under these conditions, wall roughness influences the flow greatly and is thus an essential input for any CFD simulation, even if this means accepting the default roughness values supplied by the CFD software's manufacturer, especially when modelling a water-only flow. This paper aims to measure the wall properties of a mineral separation spiral and to the best of the authors' knowledge, no such wall roughness data have been published to date.

A further aspect of the wall-fluid interaction, and a fluid simulation input that must be defined, is the wall-fluid-air contact angle, henceforth referred to as the 'wall contact angle'. This parameter, important in various fields of research [29], describes the interaction of water with a surface. A large wall contact angle defines a hydrophobic wall surface and causes a deposited water droplet to form a bead. A low wall contact angle defines a hydrophilic surface and causes a deposited water droplet to spread out and wet the surface to a greater extent. Holtham [24] showed the importance of this wall contact angle in water-only flows by collecting experimental measurements before and after the application of hydrophilic paint to the trough, since such paint changes the wall contact angle. Before application of the paint, a water-only flow would only partially wet the trough near the outer diameter, whereas after painting the inner regions of the trough were also wetted. The artificially altered wall contact angle acting on the thin water region pulled the start of the water free surface inwards, resulting in a complete wetting of the trough. This makes clear that to accurately validate the simplest flow in a spiral, a water-only flow, knowledge of a realistic wall contact angle is an essential variable in a CFD simulation. Therefore, this variable must either be purposefully defined by a user or naively left as the software's default value. However, although a simulation needs this variable to be input, systematic guidance on defining such wall contact angle of an unmodified spiral surface does not appear to have been published.

A final aspect of the important wall-fluid interaction is to accurately reflect the shape of the trough in the fluid flow simulation. The helical base shape of a spiral can be distorted by the influence of manufacturing processes and gravitational forces. To this end, the exact shape of the trough is measured at six locations along the length of an upright, production-ready spiral.

Mineral separation spirals have been developed for well over 100 years [1]. It is not surprising that different spiral manufacturers have progressed their spiral design along similar lines. The fact that various spiral manufacturers have adopted polyurethane as their spirals' wear layer [30-32] is testament to this design process as well as to the excellent wear properties of this material. This general application of a polyurethane wear layer in spiral separators makes the presented measurements applicable to a wide variety of spiral makes and models.

A clearly-defined line of entrained air bubbles, henceforth referred to as the 'bubble line', is often encountered in industrial applications of mineral separation spirals, as shown in Figure 2.

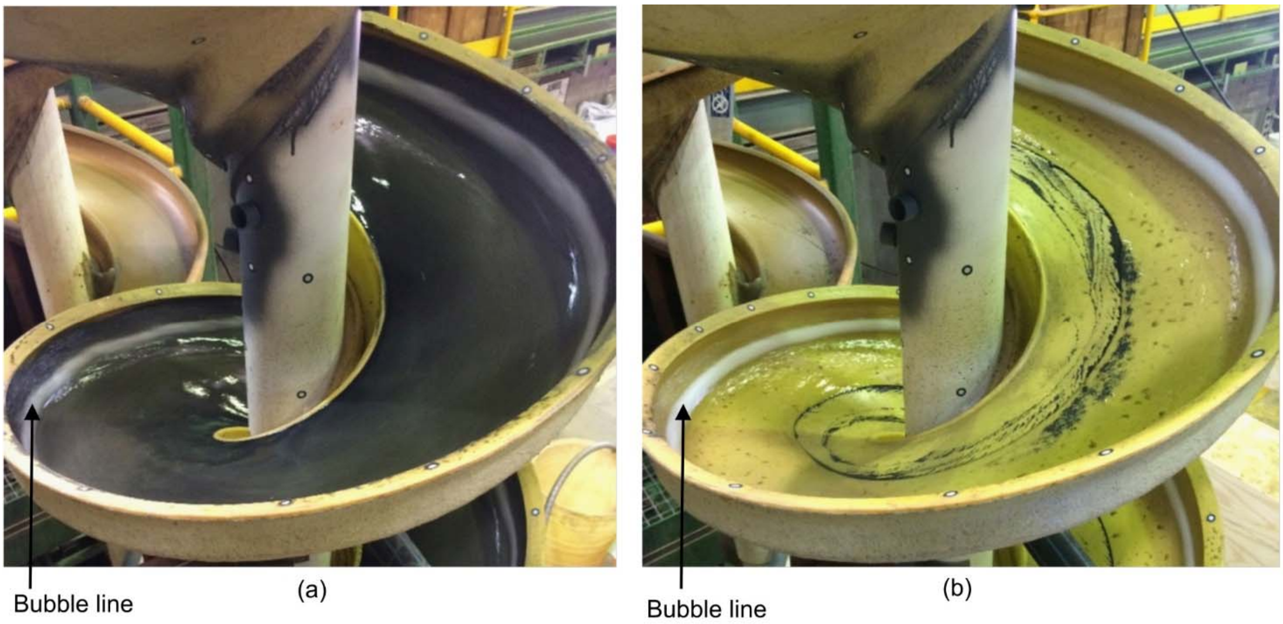

Figure 2: Bubble line in a mineral separation spiral with a chromite dominated slurry (a) and water-only flow (b)

The bubble line has not been the subject of significant research efforts. Palmer et al. [2] theorised that the bubble line could be the result of various interacting flows [2]. Jain & Rayasam [6] suggested that the bubble line is indicative of high turbulence where 'water at the periphery reaches escape point and spins back on the trough due to its curved profile. The splashing back of water is subdued because of the continuous flow of water and is observed as a continuous line of fine bubbles running down along the periphery of spiral trough'*.* Given the common occurrence of the bubble line, general observations thereof can be used qualitatively in other spiral makes and models.

2 Materials and Methods

This section describes the measurement of the wall roughness, the wall contact angle, the trough surface, the free surface, and the bubble line size and position of a full-scale operational CS1-type spiral running a water-only flow and two slurry flows.

All measurements were conducted on a so-called 'wetted-in' spiral. During the manufacturing of the trough, a release agent is applied to the mould to aid in the demoulding process. This release agent is hydrophobic, adheres to the demoulded trough and has the potential to affect the location and shape of the water free surface [24], the wall roughness and wall contact angle. When water or a slurry has worn the release agent away, the spiral is said to be 'wetted-in'. Prior to the experimental measurements described in this research paper, the spiral was run continuously for 7 days with an abrasive iron ore slurry to ensure any release agent residue has been worn away. The particle size distributions and particle density distributions of both slurries were measured through Heavy Liquid Separation (HLS) and are given in Table 1 and Table 2.

Chromite slurry		**Magnetite slurry**	
Size (µm)	**Percentage (%) by weight**	**Size (µm)**	**Percentage (%) by weight**
+850	1.5		
-850+500	5.1	+500	0.5
-500+250	24.8	-500+250	14.9
-250+150	28.6	-250+150	46.2
-150+106	13.1	-150+75	35.5
-106+75	9.5		
-75+38	10.7	-75+38	2.1
-38+20	2.9	-38+20	0.2
-20	3.7	-20	0.6
Total	100.0	**Total**	100.0
D50 (µm):	*185*	*D50 (µm):*	*175*

Table 1: The particle size distribution of the chromite and magnetite slurries

Chromite slurry			**Magnetite slurry**		
Size Fraction	**Specific Gravity (SG) of the fraction**	**rcentage (%) by weight**	**Size Fraction**	**Specific Gravity (SG) of the fraction**	**rcentage (%) by weight**
+20µm	-2.85	9.2	+20µm	-2.85	3.7
	+2.85 -3.6	38.6		+2.85 -3.6	22.8
	+3.6 -4.05	6.5		+3.6 -4.05	1.3
	+4.05	41.9		+4.05	71.6
	sub -total	*96.3*		*sub -total*	*99.4*
-20µm	-	3.7	-20µm	-	0.6
Total	-	100.0	**Total**	-	100.0

Table 2: The density profile of the chromite and magnetite slurries

2.1 Specimen preparation

Normally a spiral trough consists of a polyurethane wear layer which, due to its flexible nature, needs to be supported by a structural layer to withstand the forces of gravity and the moving slurry. Due to the curvature of the spiral in two directions, one being the downwards helix, and the other being the curved cross-sectional shape, specimens extracted from any location on a spiral would not be flat and could not be flattened due to the inseparable rigid structural layer. This poses a problem in wall roughness and contact angle testing as a flat or slightly uneven specimen is preferred to prevent distortion of the measurements. This issue was circumvented by introducing a sacrificial wear layer.

A sacrificial wear layer, without the rigid support layer, was produced using the same mould for a normal dual-layered spiral. This sacrificial wear layer is made from the same polyurethane as the original wear layer. Figure 3 shows how this layer was cut to size and overlaid onto the CS1 spiral, then attached to the spiral using screws in unobtrusive locations so they did not interact with the fluid flow. The centripetal force of the moving water and slurries ensured that the outer diameter of the sacrificial wear layer was forced into the shape of the existing wear layer. The feed box was attached on top of the sacrificial wear layer to ensure that the transition from the feed box onto the spiral trough was not altered. The sacrificial wear layer stopped before the product box and thus introduced a disturbance to the flow at this location, possibly altering the mineral separation performance. However, since the spiral's separation performance is not a subject of investigation in this research paper, and this disturbance is not located in the vicinity of the six free surface measurement locations, this transition does not affect any measurements or conclusions. After running the spirals for the prescribed time, the flexible sacrificial wear layer was removed from the spiral and specimens were then extracted from it. This approach thus resulted in specimens of the wear layer of a mineral separation spiral that were worn under realistic flow conditions and were able to be flattened for the roughness and wall contact angle measurements.

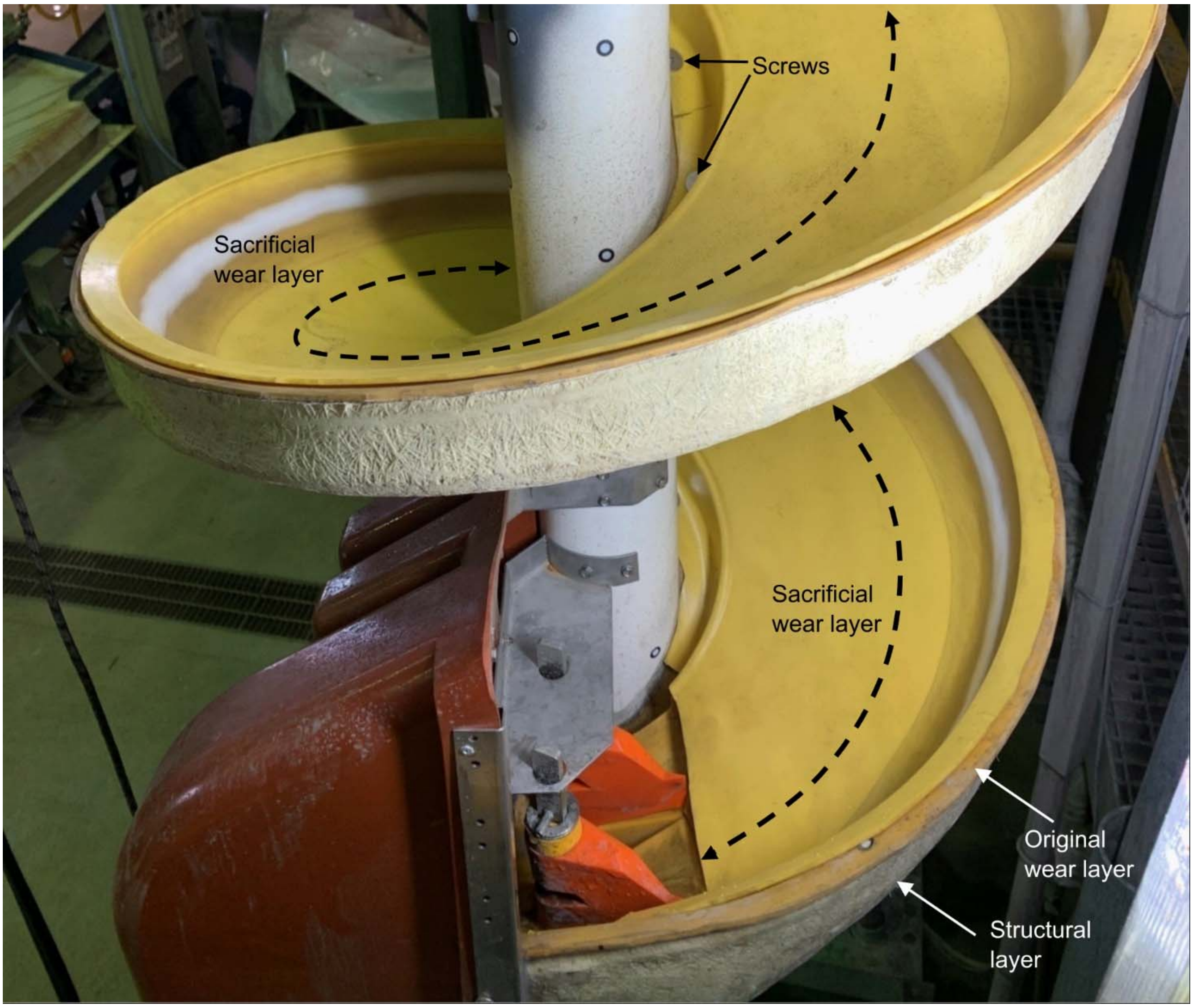

Figure 3: Sacrificial wear layer installed on the CS1 spiral.

To derive a representative average roughness of the trough surface, specimens are needed from multiple locations. Three locations were selected where the iron ore slurry contacted the trough during the wetting-in process, Location A, B and C in Figure 4. A further location, where the slurry flow never touched the trough, Location D in Figure 4, was selected as a control. Specimens measuring 10 mm × 50 mm were cut using scissors where the long dimension of the specimen was cut to follow the curvature of the spiral. The extracted specimens were used in subsequent experiments to measure the wall roughness and wall contact angle.

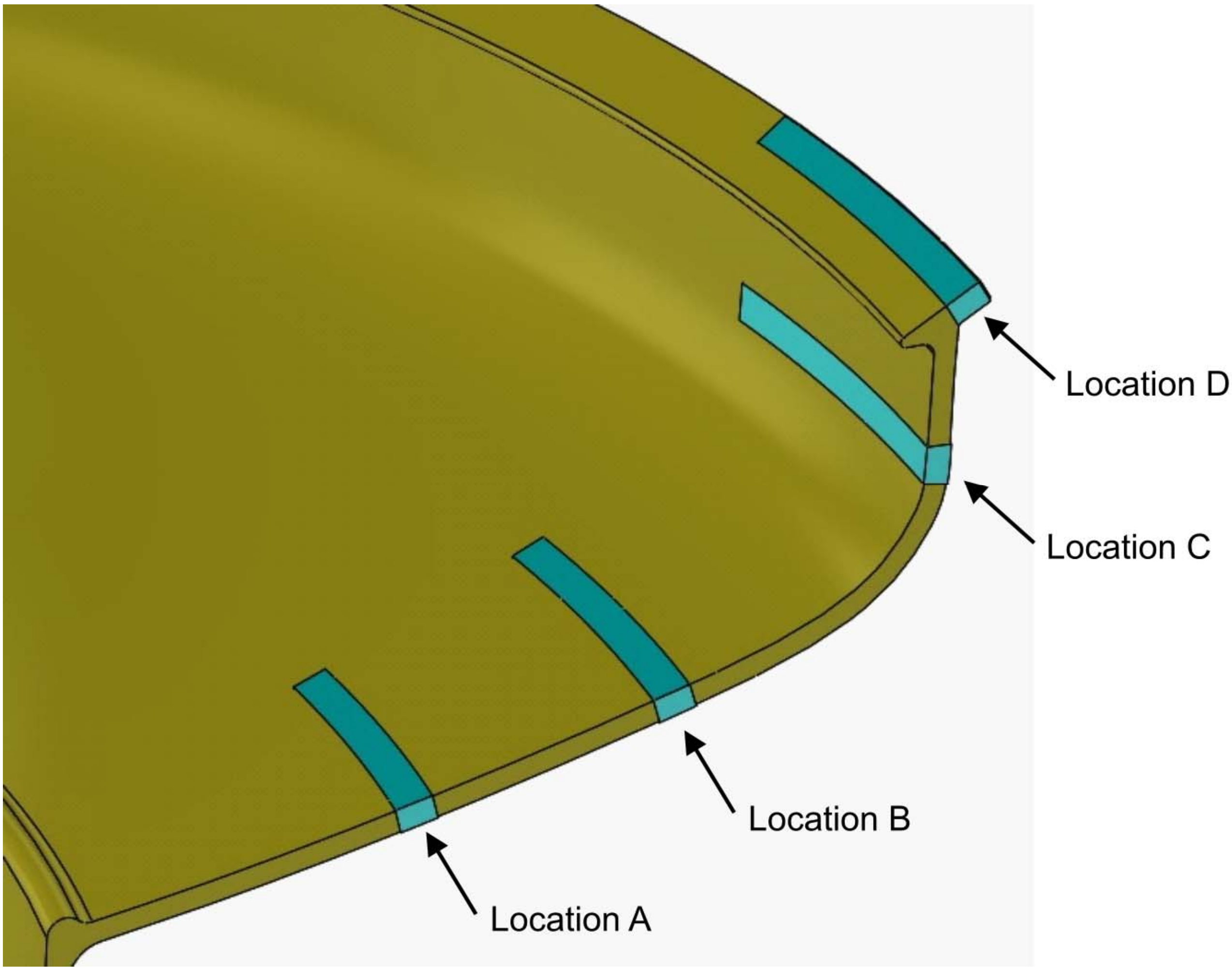

Figure 4: Location on the spiral trough of the extracted specimens

2.2 Surface roughness measurements

For the roughness measurements, the specimens described in section 2.1 were affixed to a flat aluminium backing plate using ‘Blu-Tack’, a putty-like adhesive. This allowed the top surface to be positioned parallel to the horizontal plane to the best of the operator’s ability, as shown in Figure 5.

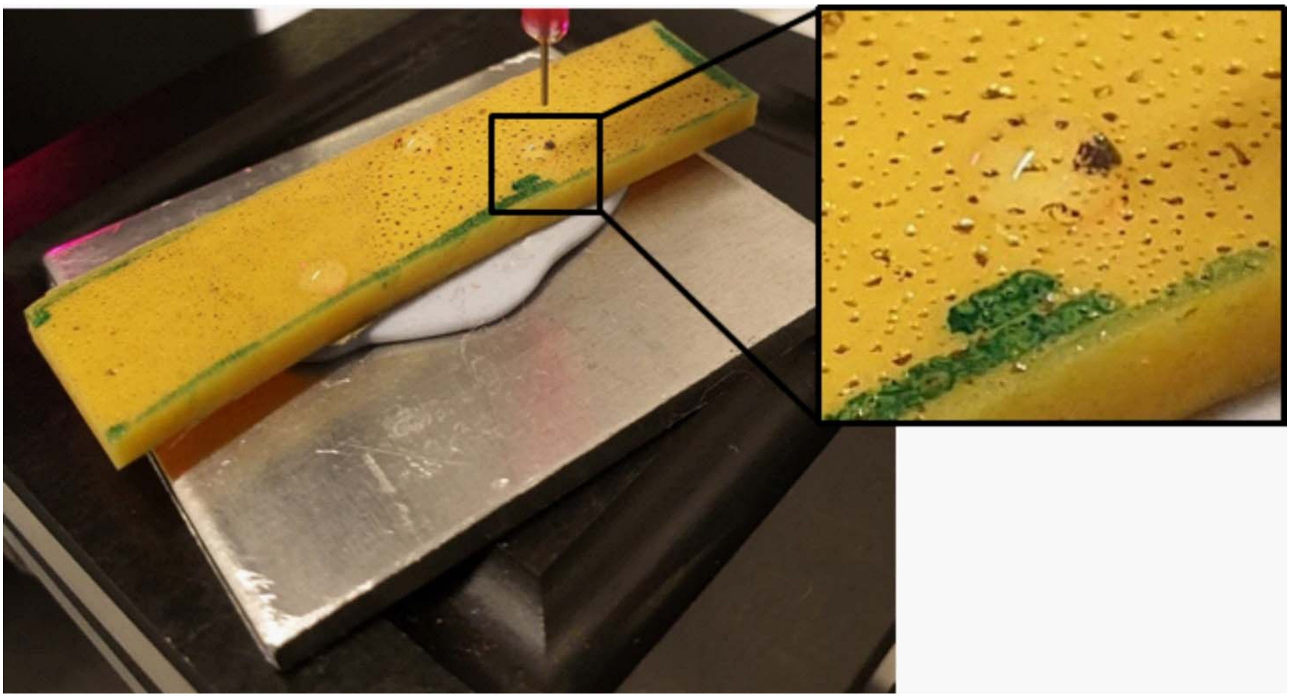

Figure 5: A trough specimen affixed to a flat aluminium backing plate using ‘Blu-Tack’ adhesive, and a zoomed in view of the specimen’s surface porosity

The surface was scanned with an Olympus OLS5000 3D measuring laser microscope using a 10× zoom level on a 10 × 10 mm portion of each specimen. To correct any remaining curvature a digital second-order polynomial curvature correction was utilised. Tilt correction was applied to digitally level the specimens. Digital noise correction was utilised during the scan. Roughness values were determined by digitally assessing, and averaging, the topology height along a minimum of 6 equally spaced, parallel lines across the 10 x 10 mm scan area. Two roughness values were reported: the commonly used Arithmetic Mean Deviation (Ra), and the Maximum Height (Rz).

Due to the porosity of the specimen, the potential exists that iron ore particles imbed or become lodged in cavities along the trough top surface. Care was thus taken to not clean the specimens before testing in order to capture, as realistically as possible, the surface roughness of the trough as experienced by a moving slurry and water flow. The surface porosity of the specimen is highlighted by the iron ore residue forming black dots that can be observed in the inset zoomed-in view of Figure 5.

2.3 Wall contact angle measurements

The same specimens used in the roughness measurements were placed in the Biolin Scientific Attension Theta Flex Optical Tensiometer to perform wall contact angle measurements. Specimen levelling was achieved via the manually operated tilt frame so that the surface was flat from the tensiometer camera's viewpoint, as shown in Figure 6.

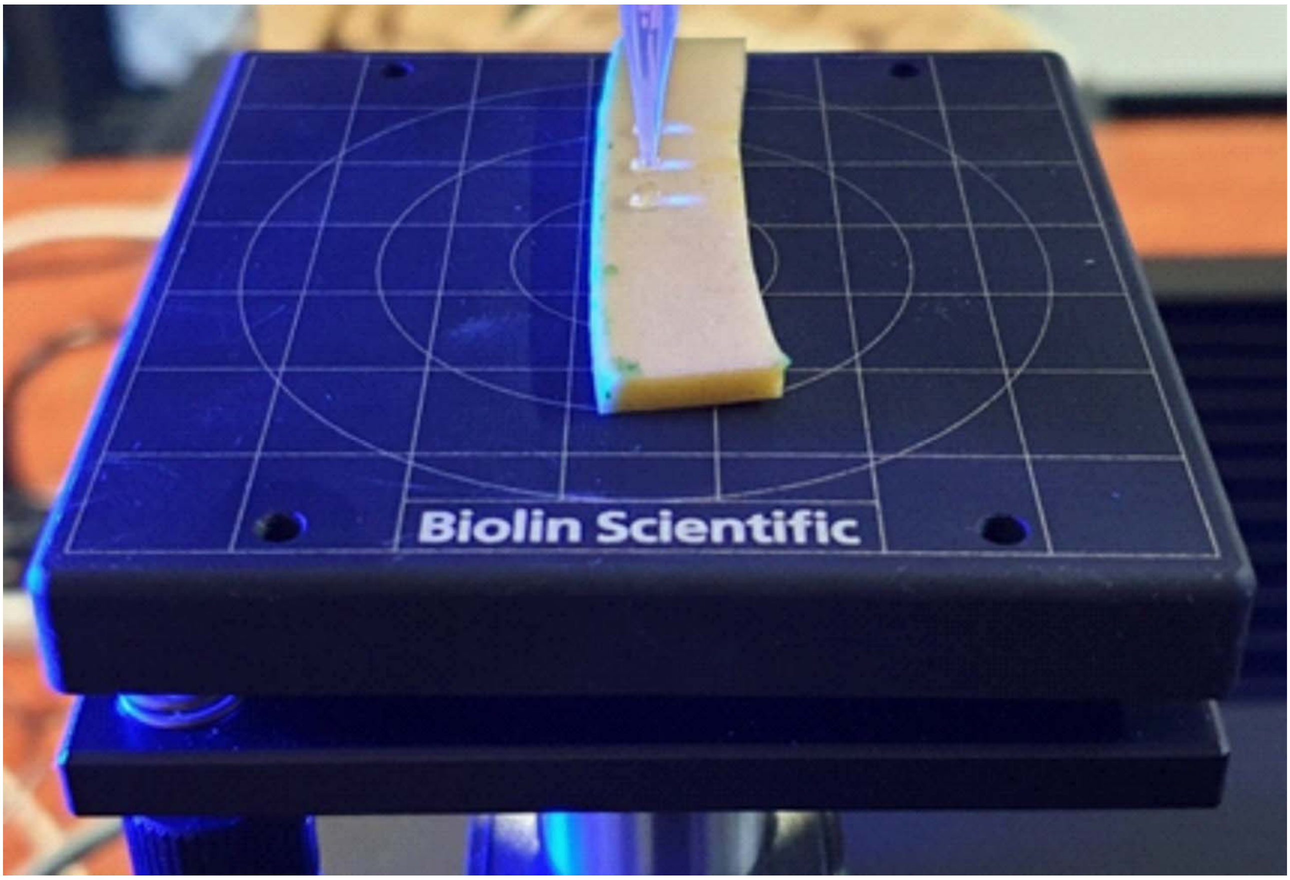

Figure 6: The specimen levelled using the tilt mechanism on the tensiometer, the syringe has just deposited the third sessile drop

For each specimen, the height of the specimen tilt frame was entered in the tensiometer software, as was the specimen thickness. This allowed the software to set an appropriate starting position of the syringe tip. Default software settings were used, including positioning the camera to minus 2° to allow the capture of the droplet's reflection on the specimen. With these settings, the tensiometer was set to run a sessile drop experiment, where firstly an automatically dispensed droplet made from 5 microliters of distilled water was suspended at the syringe tip. The syringe, and thus the suspended droplet, were then automatically lowered, based on the specimen thickness and tilt frame settings, so that the droplet contacts the specimen surface, wetting it partially. The syringe was subsequently raised, which forced the droplet to detach from the syringe tip and completely wet the surface. Once the syringe started its ascent, 10 s of video was recorded at 33 frames per second. For each specimen (Location A, B, C and D) a minimum of 3 sessile drop experiments were performed via this procedure.

The wall contact angle is calculated through post-processing of the recorded video using the tensiometer data analysis software. Default Young-Laplace curve fitting is used to automatically approximate the curvature of the droplet mathematically. This curvature is intersected by a horizontal line determined by the specimen surface, the so-called 'baseline'. For each individual sessile drop test, the baseline was set to where the bubble curvature meets its reflection, as captured by the camera. At the two intersection points of the baseline with the droplet curvature, on both sides of the droplet, the software calculates the wall contact angle, measured inside the water phase. As the bubble needs to settle after the removal of the syringe tip, the wall contact angle was calculated for every frame once the change in angle is less than 0.15%. At each frame, the resulting wall contact angles were exported from the tensiometer software and averaged over both time and the readings from the two sides of the droplet.

2.4 Free surface and bubble line measurements

Measurements on the flow behaviour of a CS1 mineral separation spiral were conducted for a water-only flow at a flow rate of 6.3 m^3/hr, a Chromite slurry at a flow rate of 7.9 m^3/hr with a 46.2% solids content, and a Magnetite slurry at a flow rate of 7.9 m^3/hr with a 45.7% solids content. Measurements of the free surface of the water-only and slurry flows were taken using a bespoke free surface sampling jig. The jig is based on a design proposed by Holland-Batt [4], which was also applied by Loveday [17], but has been improved upon to match the curvature of the CS1 to ensure the most accurate fit and ease of measurements. The 3D printed free surface sampling jig is shown in Figure 7. #

Once a steady state flow was reached, the jig was positioned above the trough by aligning the curved surface to the outside of the column. The end tap was placed on the trough lip and secured, and adjustment of the jacking screw ensured that the spirit level showed no out-of-plane positioning of the jig. The sampling probes were subsequently lowered to intermittently touch the free surface of the water or slurry. Intermittent contact is important as ‘steady contact would tend to underestimate the flow depth’ [4]. Once the probes were positioned correctly, the jig was removed while ensuring the probes remained fixed in place. Measurements were then taken from the top of the probe to the bottom of the jig along the axis of each probe. These measurements were recorded and copied to the 3D CAD model of the jig, which, through the known length of each probe, determined the position of each probe tip relative to the jig. To relate the position of the jig to the trough, the probe closest to the column was always brought into contact with the trough surface.

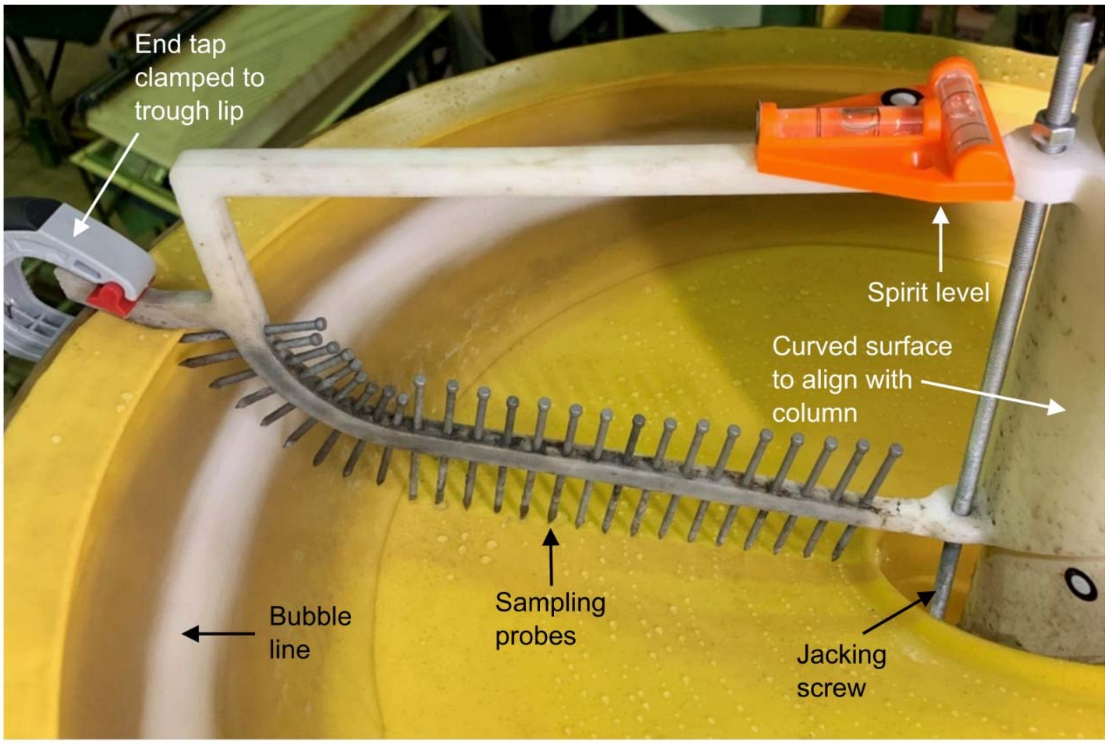

(a)

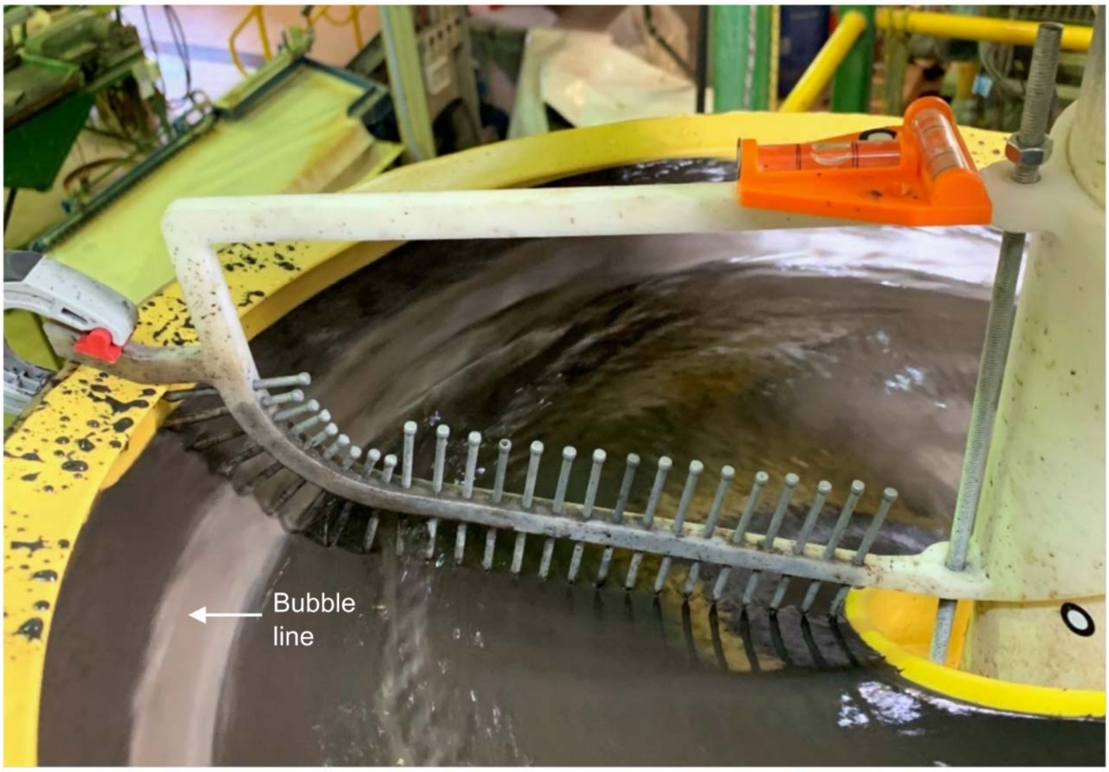

(b)

Figure 7: 3D printed free surface sampling jig for the CS1 spiral applied to the water (a) and iron ore slurry (b) flows

The bubble line is clearly visible in Figure 7 and the sampling jig was also used to record the position and width of this bubble line, supported by the assessment of slow-motion video footage of the experiments.

Six sampling locations along the spiral trough were selected to measure the free surface and the bubble line position and width, as shown in Figure 8.

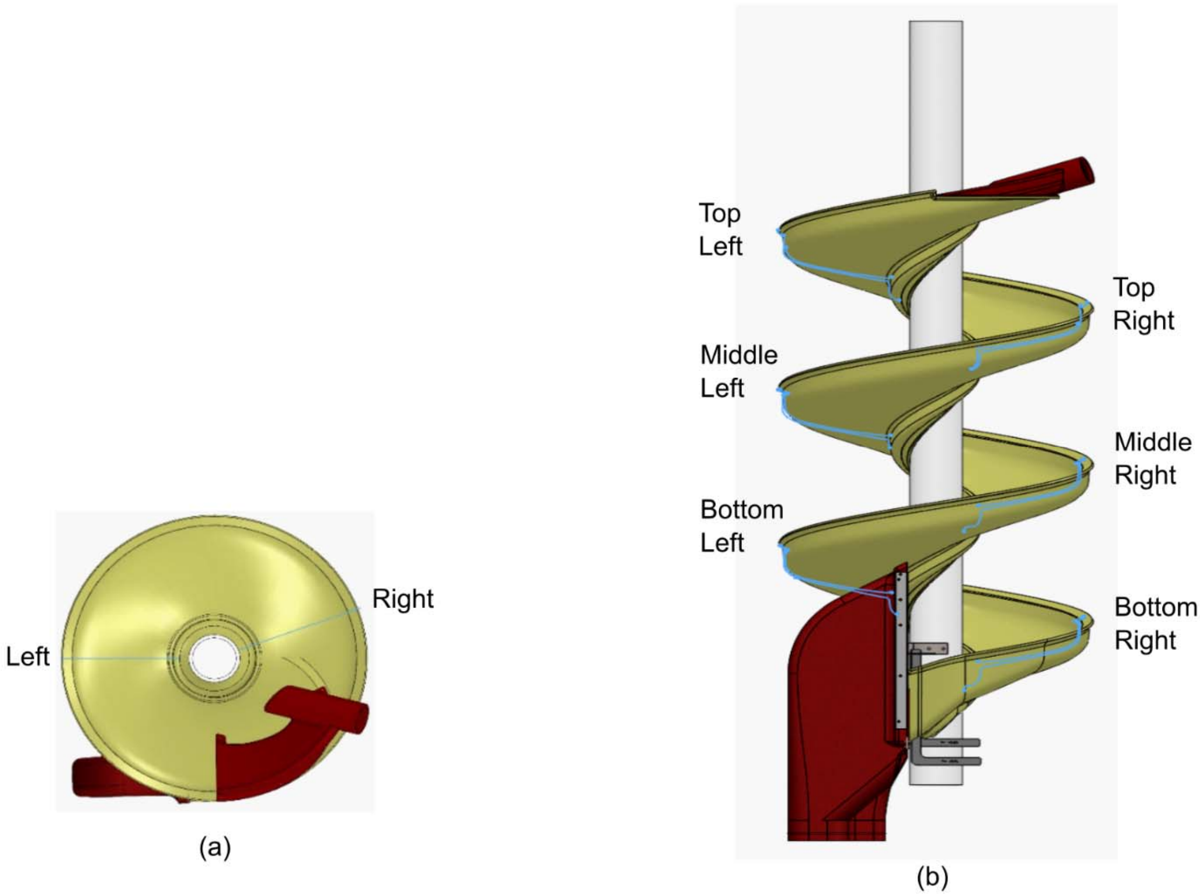

Figure 8: Top view (a) and front view (b) of the six sampling locations on the CS1 spiral

2.5 Trough surface profile measurements

Measurements of the shape of the water free surface and location of the bubble line would be meaningless without firstly measuring the trough surface to which these measurements can be related. Although a 3D CAD model of the CS1 spiral exists, this model was only used to produce the mould onto which the spiral was created. Therefore, the existing CAD model does not account for shrinkage that occurs during the trough's curing process. Additionally, when attaching the trough to the column, the trough is stretched to achieve the desired pitch. Furthermore, gravitational forces deform the trough when it is mounted upright. As such, a 3D CAD model cannot be relied upon to represent an assembled, production-ready, upright spiral.

To capture the accurate shape of the trough, the sampling jigs were used to determine the shape of the empty sacrificial wear layer at the same six sampling locations listed in Figure 8.

2.6 Bubble origin assessment

To assess the origin of the bubbles in the spiral, a see-through feed box was manufactured and utilised during testing. This allowed the opportunity to gauge whether the bubble line is created by entraining air in the water flow along the trough or if the bubbles are already present at the inlet of the feed box.

3 Experimental Results

3.1 Surface roughness measurements

The porosity of the specimen's top surface varied greatly along the spiral trough. In fact, the distribution of black dots in Figure 5 make it clear that the porosity is not uniform along individual specimens. To assess the porosity along the specimen thickness, a 1.8 × 1.8 mm scan of the side of Location D was performed using a 20× zoom. The result of this scan is shown in Figure 9 where the top of the specimen corresponds to the top of the image.

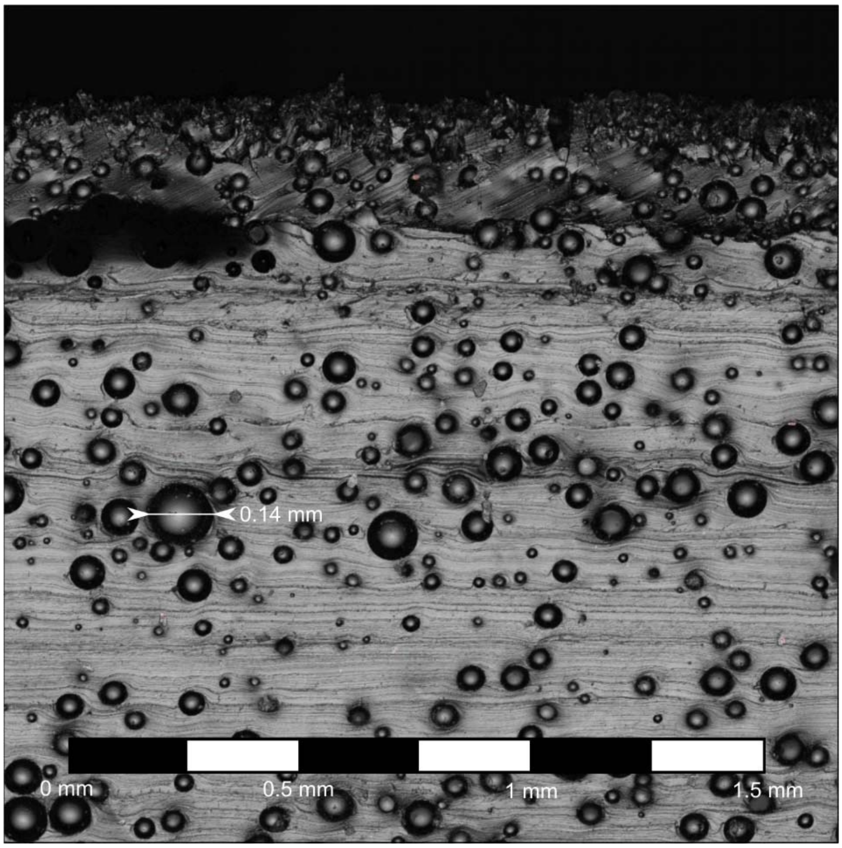

Figure 9: Microscopic 1.8 mm × 1.8 mm scan of the side of Location D

This cross-sectional view shows that the porosity varies throughout the specimen thickness and the large variations in surface porosity, shown in Figure 5 are thus unsurprising. It is believed that the porosity results from the manufacturing process of the polyurethane layer or is a consequence of its curing process, or both.

To account for the large differences in porosity, a scan area measuring 10 mm × 10 mm was selected as being the most representative of each specimen location. Given the 10 mm × 50 mm specimen dimensions, the scan areas captured 20% of each specimen's surface area. The scan areas were thus a large, representative area of each specimen's surface area. Six independent roughness measurements were taken, and averaged, ensuring that each measured roughness value was representative of each location.

The large range of porosity differences is evident in Figure 10 which shows the scan area of all four Locations (A,B,C and D), acquired through the Olympus OLS5000 3D measuring laser microscope, all at a 10× zoom level.

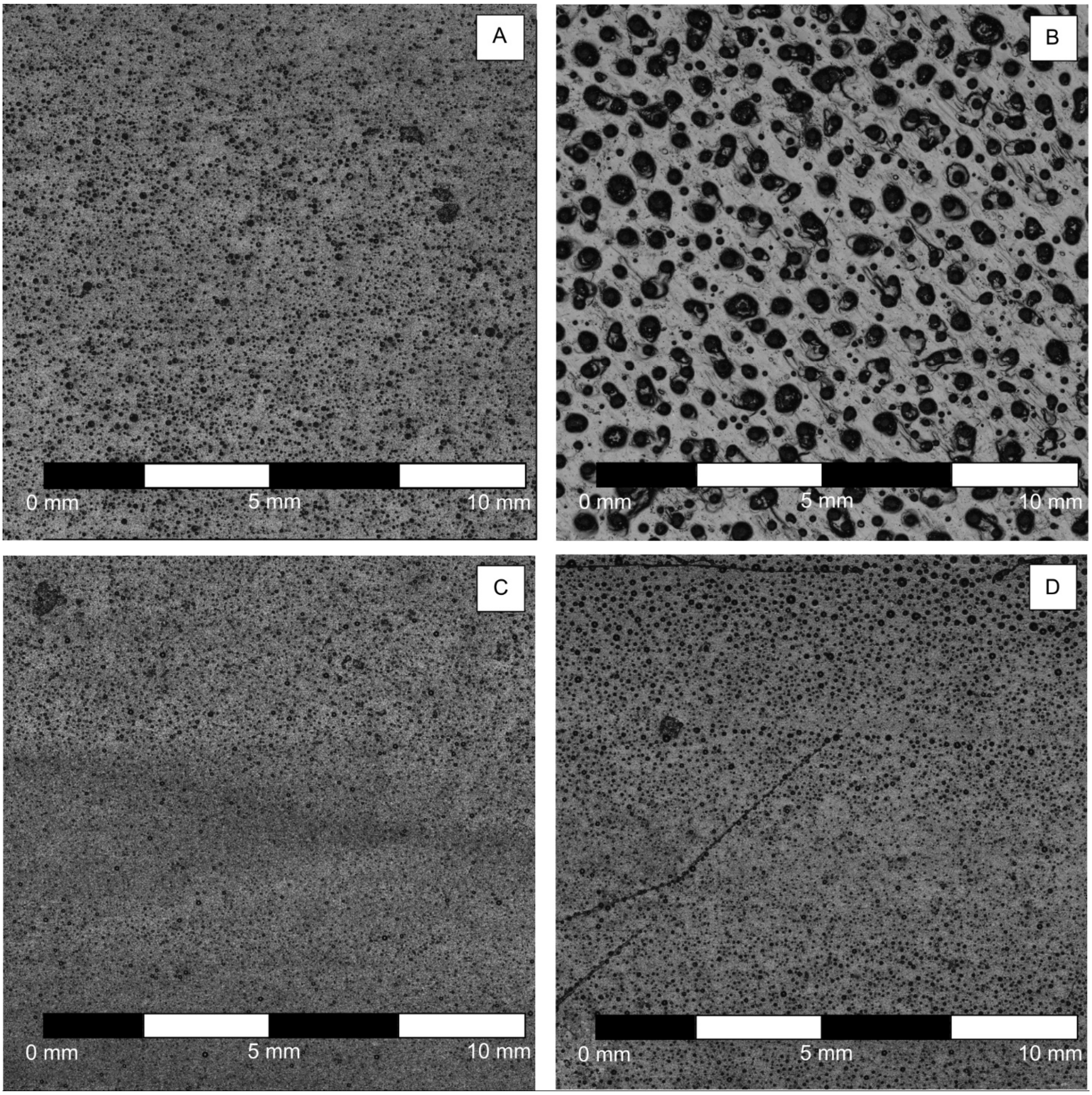

Figure 10: Microscopic images of a representative 10 mm × 10 mm scan area of Location A, B, C and D

Noticeable is the scan area of Location B, where the pores are much larger than those found at the other Locations. These porosity differences are reflected in the Arithmetic Mean Deviation (Ra) per Location, including the standard deviation.

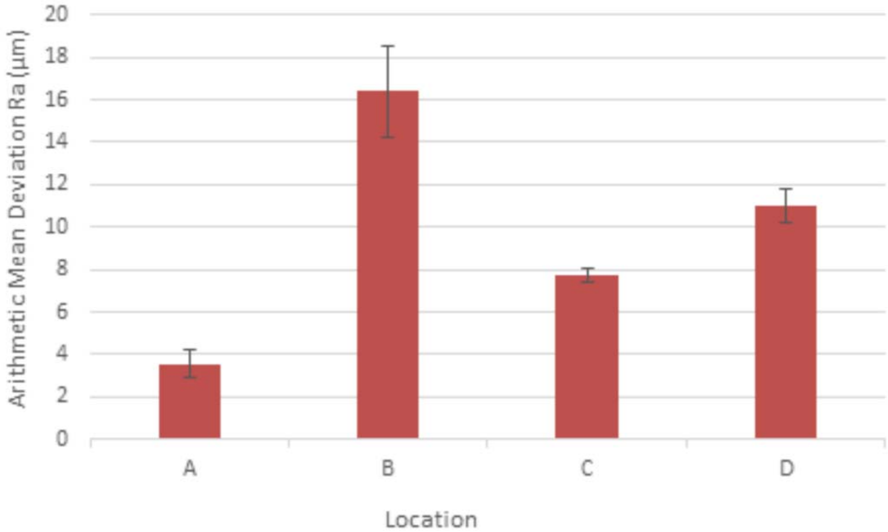

Figure 11: Averaged Arithmetic Mean Deviation (Ra), and its deviation, for the scanned areas of Location A, B, C and D

The Maximum Roughness Height (Rz) metric is less sensitive to the porosity as it focusses on the deepest and highest parts of the scan area. The resulting roughness values of the same scan areas shown in Figure 10 are given in Figure 12. The results indicate that the Rz values fluctuate less over the specimens than the Ra roughness metric.

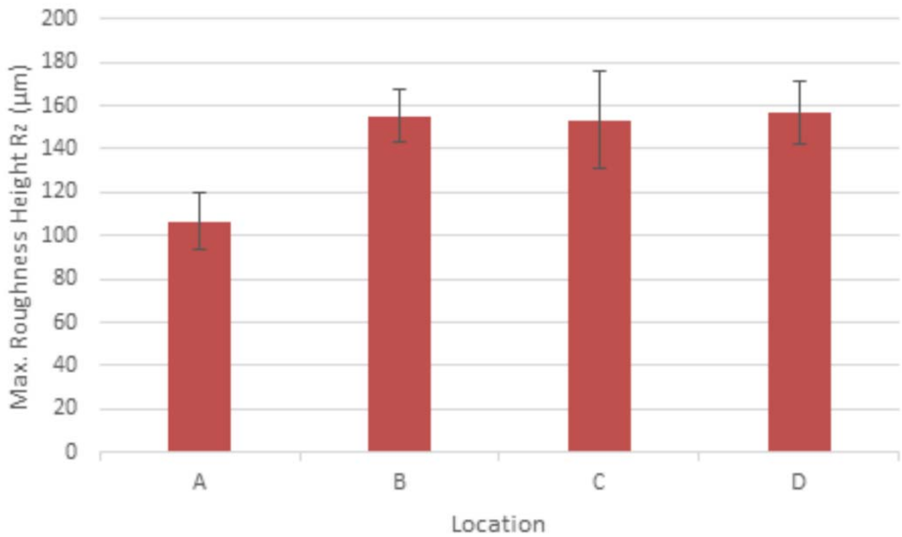

Figure 12: Averaged Maximum Roughness Height (Rz), and its standard deviation, for the scanned areas of Location A, B, C and D

The averaged Arithmetic Mean Deviation (Ra), Maximum Roughness Height (Rz), and their respective standard deviation, averaged over the wetted-in Locations (A, B and C) and the non-wetted-in Location D are given in Table 3.

	Trough surface	
	Wetted-in	Non-wetted-in
Arithmetic Mean Deviation (Ra)	9.2 µm (5.5)	11.0 µm (0.8)
Maximum Roughness Height (Rz)	138.4 µm (27.9)	156.7 µm (14.47)

Table 3: The roughness values and wall contact angle of the wetted-in versus the non-wetted-in trough surface

3.2 Wall contact angle measurements

For each video recording of a sessile drop test, the baseline was determined in a post-processing step. A correctly set baseline is shown in Figure 13 where, next to the reflection of the droplet itself, the reflection of impurities on the specimen surface were used to position the baseline. At the intersection of the baseline with the curvature of the droplet, the wall contact angle was determined. These wall angle calculation points are highlighted in Figure 13.

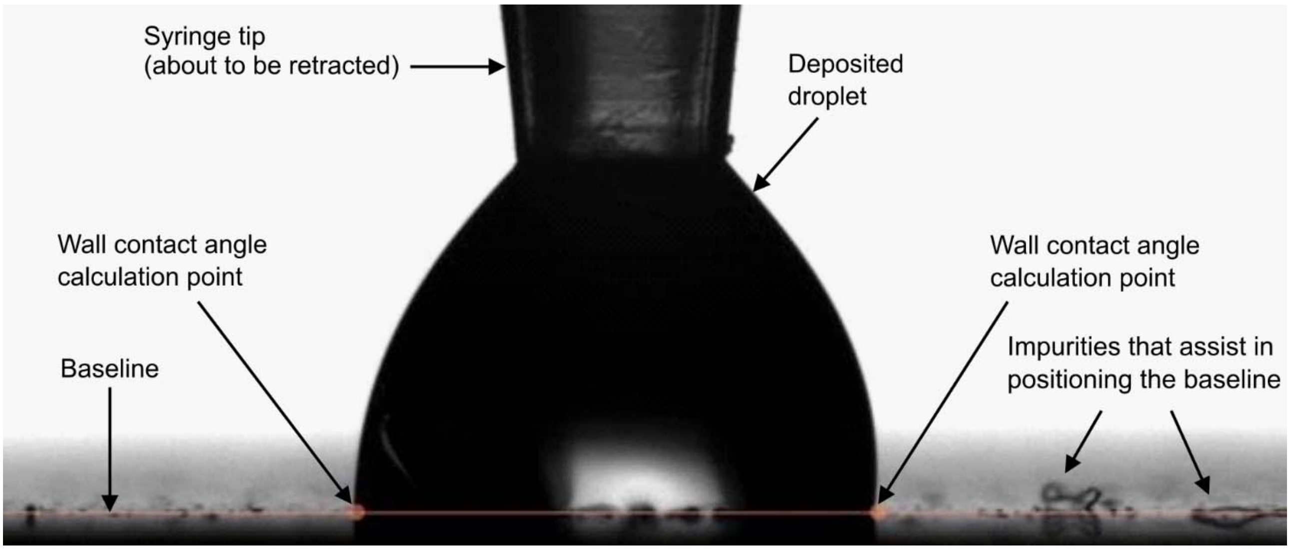

Figure 13: An example of a correctly set baseline

In Figure 13, the droplet had been brought into contact with the surface while still connected to the syringe tip, following the sequence described Section 2.3. Subsequently, the syringe tip was retracted, leaving the droplet to settle, and fully wet the surface. During this settling process the droplet was seen to wobble left and right in several drop tests indicating that new pores were being wetted. This wobbling settled over time and the droplet reached a steady state. From this point onwards, the wall contact angle was measured in the water phase at both calculation points.

The resulting wall contact angle is shown in Figure 14 averaged over three separate data ranges:

time, two calculation points, and at least three drops per specimen.

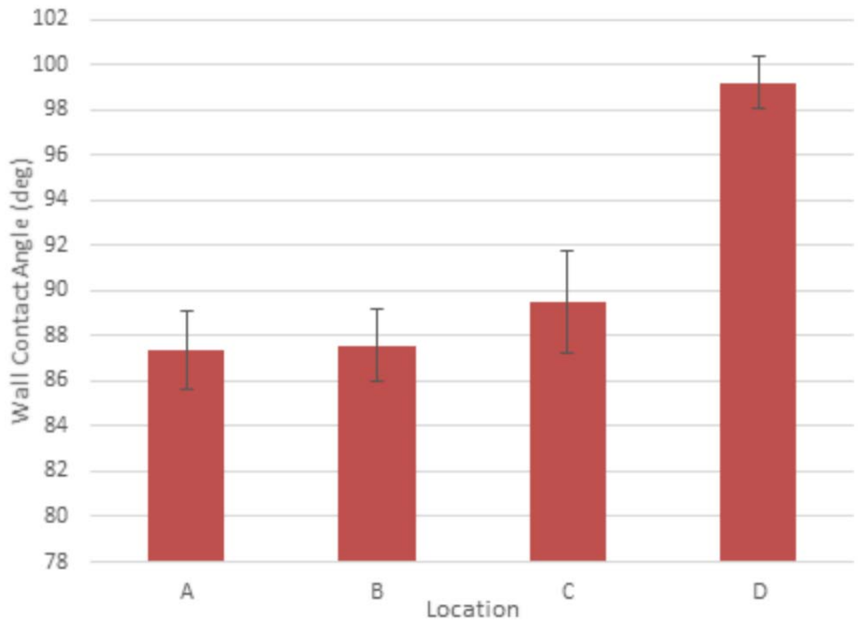

Figure 14: Averaged wall contact angle, and its standard deviation, for Location A, B, C and D

The wall contact angle overview shows a clear distinction between Location A, B and C, where an iron ore slurry has 'wetted-in' the trough, and Location D, which did not interact with a slurry. It can thus be reasoned that the release agent, once covering the whole of the spiral trough, has been worn away by the iron ore slurry at Location A, B and C, whereas Location D still has this hydrophobic layer applied. The wall contact angles and their standard deviations, averaged over the wetted-in Locations (A, B and C) and the non-wetted-in Location D are given in Table 4.

	Trough surface	
	Wetted-in	**Non-wetted-in**
Wall contact angle (measured in the water phase)	88.14° (0.95)	99.20° (4.68)

Table 4: The wall contact angle of the wetted-in versus the non-wetted-in trough surface

3.3 Free surface and bubble line measurements

3.3.1 Water free surface

The water free surface shapes at each of the six sampling locations are shown in red in Figure 15 overlaid onto the empty trough surface measurements. The portion of the trough with the smallest radius will be referred to as the 'inside' of the trough, and the portion of the trough with the largest radius is henceforth referred to as the 'outside' of the trough.

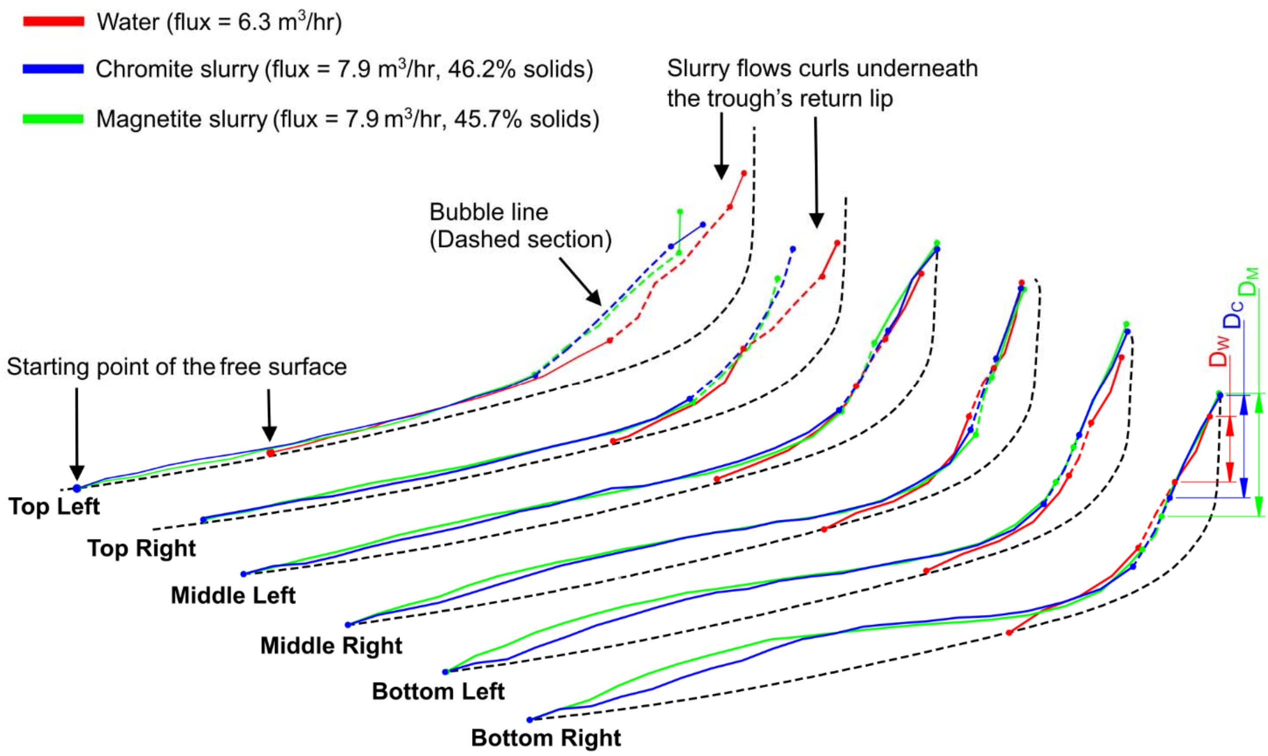

Figure 15: Free surface at the six sampling locations including the position and width of the bubble line for a water flow, a Chromite slurry, and a Magnetite slurry

The Top Left and Top Right profiles show an open free surface at the outside of the trough. As the water and slurries flowed from the feed box onto the trough, the free curve curled up underneath the trough's overhanging return lip, visible in Figure 16 (a) by a clearly retracted top probe. As the flow turbulence reduces when moving down the spiral, this effect disappeared in later sampling locations.

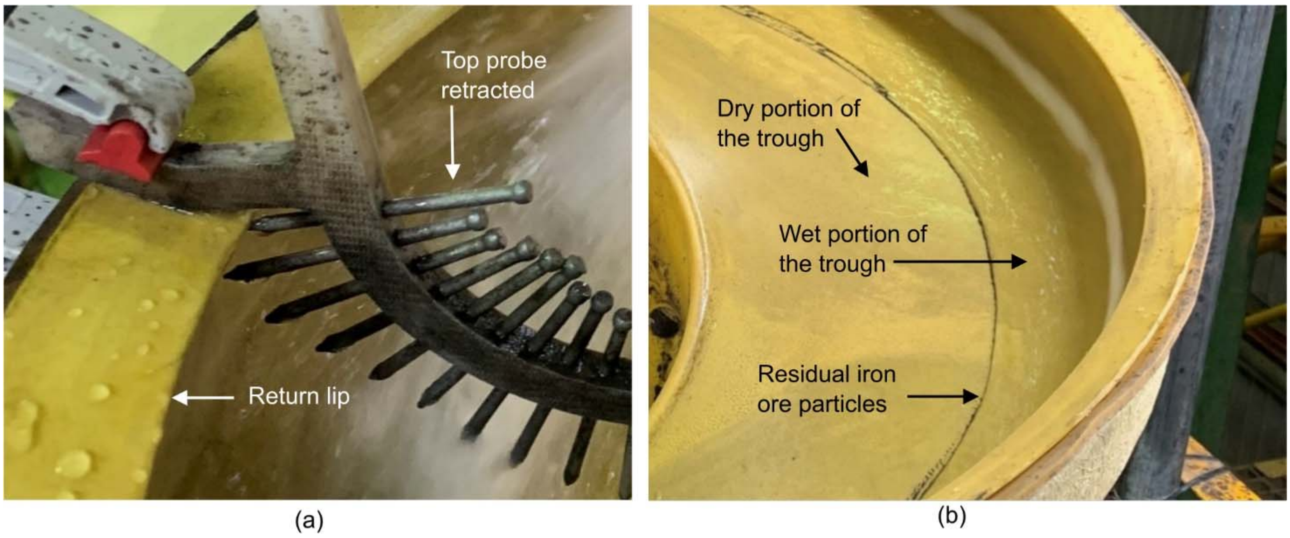

Figure 16: Water curling underneath the return lip at the Top Left sampling location (a). Partial wetting of the trough (b)

The free surface measurements indicate that the water-only flow wets roughly half of the trough's 'horizontal' surface, near the outside of the trough. Figure 16 (b) clearly shows the dry and wet portions of the trough during the water-only test. The location of the start of the water free surface was marked by a black line resulting from residual iron ore particles being separated out of the water phase. The starting point of the water surface, indicated in Figure 15, only changes before the Middle Left sampling location and remains roughly consistent after that. This observation is useful in numerical fluid flow simulations, as it permits the use of a shortened fluid model, ending at the Middle Left sampling location.

Since the release agent was worn away through the wetting-in process, the release agent could not be the cause of the location of the wet-dry interface. In fact, after the free surface measurements were completed, attempts were made to wet the dry portion by intrusively altering the flow by placing an obstacle in its path. Once the obstacle was removed, the location of the wet-dry interface reverted to its previous location over time. It can thus be concluded that the incomplete wetting of the trough in a water-only flow is a feature of the flow behaviour and should therefore also be present in the results of computational fluid flow analyses.

3.3.2 Slurry free surface

The shape of the free surface of the Chromite and Magnetite slurries are shown in Figure 15 as blue and green lines respectively. The results of the empty trough surface measurements have also been incorporated into Figure 15. The start of the slurries' free surface is at the far inside of the trough and the complete spiral trough's surface is covered by the slurries. The separation effects of a spiral are evident by the continuous, and very similar, build-up of particles for both slurries near the inside of the trough. When moving from the inside towards the outside of the trough, Figure 15 clearly shows that the shape of the free surface of both slurries conform to that of the water free surface after a certain radius. A spiral separates a slurry into different streams of particles, where the larger and heavier particles move towards the inside of the trough, and the smaller and lighter particles move to the outside of the trough. It is thus believed that the free surface after a certain radius is no longer dominated by the effects of interacting particles but instead the water phase determines the shape of the free surface. It can thus be reasoned that the fluid flow after a certain radius is not governed by particles but instead relies on the fluid flow profile of water alone.

Since the shape of the slurries' free surface continuously changes when moving down the spiral, no shortened fluid model would be representable when conducting a CFD simulation of a slurry flow.

3.3.3 Bubble line analysis

The dashed section of the free surfaces in Figure 15 indicates the position and width of the bubble line. The width and position of the bubble line sees a large change before, and minimal change after the Middle Left sampling location for both the water-only and two slurry flows. Additionally, the position and size of the bubble line are similar for all three flows, further supporting the fact that water dynamics are determining the flow behaviour near the outside of the trough. The consistency of the bubble line location and positions after the Middle Left sampling location further supports the use of a shortened model in a fluid flow simulation of a water-only flow.

The vertical distance from the top of the water free surface to the start of the bubble line, indicated in Figure 15, for each flow is listed in Table 5 for the last four locations.

	Vertical distance from the highest point of the free surface to the highest point of the bubble line		
	Water (D_w)	**Chromite slurry (D_c)**	**Magnetite slurry (D_m)**
Middle Left	20.8 mm	25.9 mm	31.8 mm
Middle Right	27.2 mm	22.4 mm	28.1 mm
Bottom Left	21.0 mm	33.2 mm	29.3 mm
Bottom Right	20.8 mm	32.5 mm	39.0 mm
Average (standard dev)	**22.5 (2.7) mm**	**28.5 (4.5) mm**	**32.1 (4.2) mm**

Table 5: The bubble line position relative to the free surface shape for each flow

These measurements are in line with the observations of Palmer & Weldon where the bubble line was found to be located roughly 20 to 30mm below the highest point of the free surface [2].

An estimate of the size of the bubbles in the bubble line was challenging due to bubble coalescence and bubble bursting effects. A rough estimate was achieved by comparing the bubbles, when washed up onto the probes, to the known diameter of the probe tip before the bubbles dislodged again. Figure 17 shows a still image from the video footage taken during the water-only flow experiments where the bubbles have accumulated on the probe tip. The tip of the probe has a diameter of 0.75 mm, or 750 μm, and bubbles can be seen to have coalesced into larger sized bubbles. The smallest of these larger bubbles is still visible as indicated in Figure 17. The smallest bubble is estimated to be 1/3rd of the diameter of the probe's tip, resulting in a diameter of 250 μm for the coalesced bubbles. Still, these coalesced bubbles are surrounded by far smaller bubbles, only visible as a white foam on the probe tip in Figure 17. This leads to the estimate that the bubble size dominating the bubble line is an order of magnitude smaller than the largest visible coalesced bubble, resulting in a dominant bubble diameter of 25 μm.

Noteworthy during all experiments is the fact that no noticeable difference in bubble line velocity to the water or slurry phase velocity was found. Furthermore, the observed coalescing of bubbles on the probe's tip only occurred sporadically as newly washed-up bubbles encountered previously washed-up stationary bubbles. This indicated that the bubbles in the bubble line form a foam and bubbles do not easily coalesce. This observation was further supported by the absence of a large bubble size difference within in the bubble line.

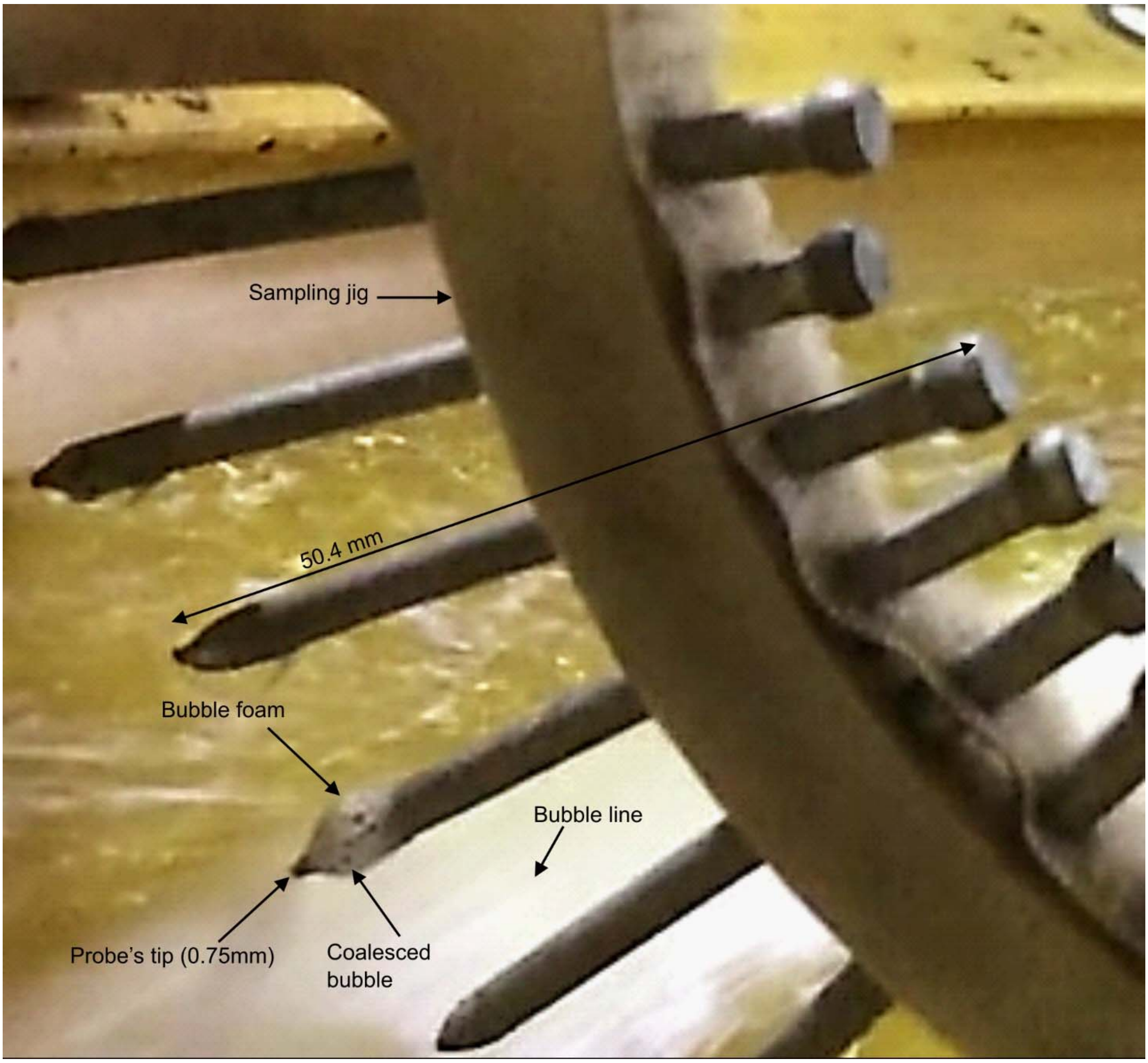

Figure 17: Still image from video footage of the experiment showing the temporary accumulation of bubbles on the probe's tip

3.5 Bubble origin assessment

Visualisation through the translucent feed box made it clear that the flow entering the feed box contained many suspended bubbles. This was most clearly visible as a white haze throughout the feed box during the water-only experiments as shown in Figure 18, with Figure 19 illustrating the viewpoint used. The presence of suspended bubbles was traced further upstream in the spiral's water supply system, as shown in Figure 20.

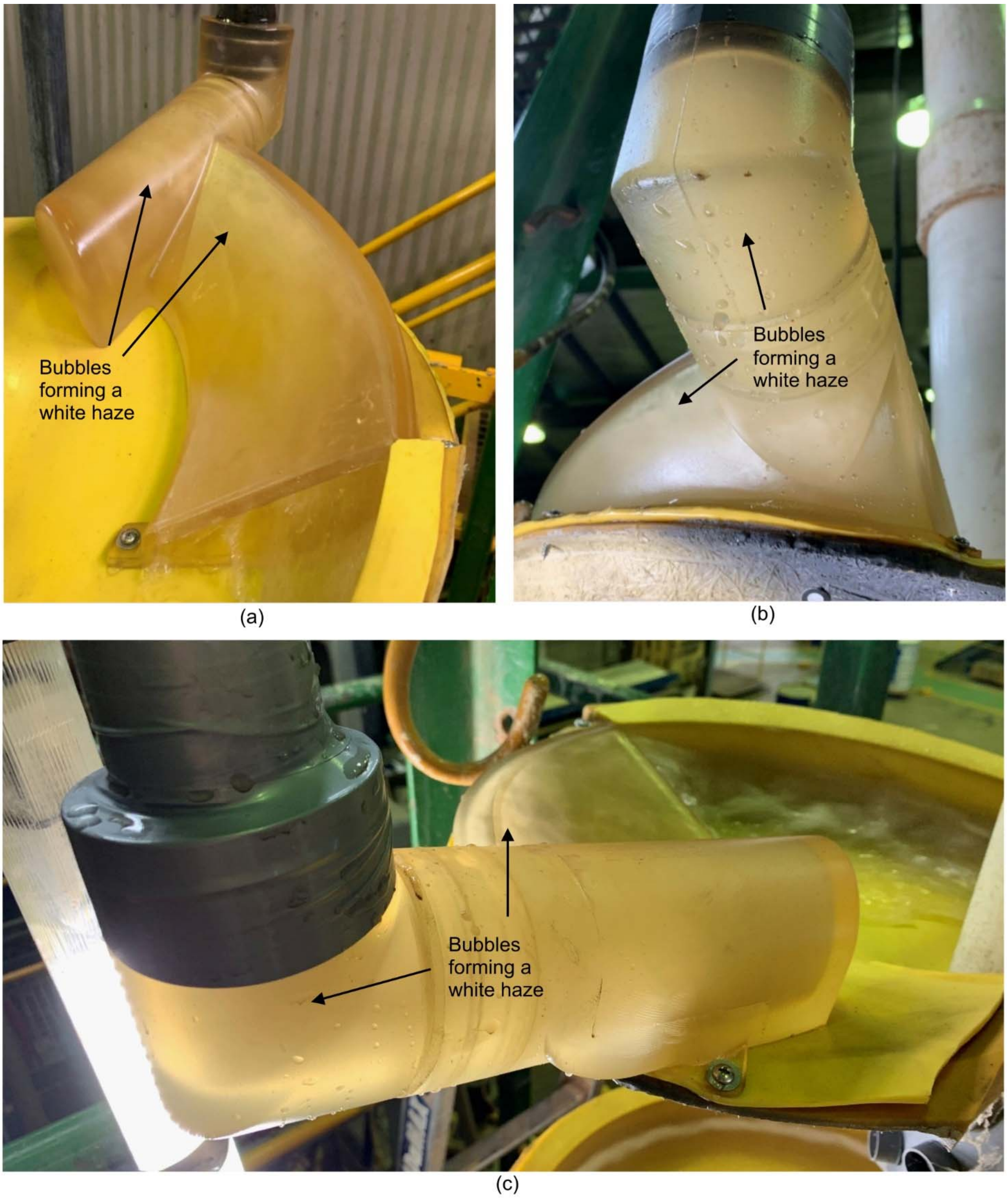

Figure 18: Top view (a), bottom view (b) and side view (c) of the flow through the feed box showing a large quantity of suspended bubbles as a white haze

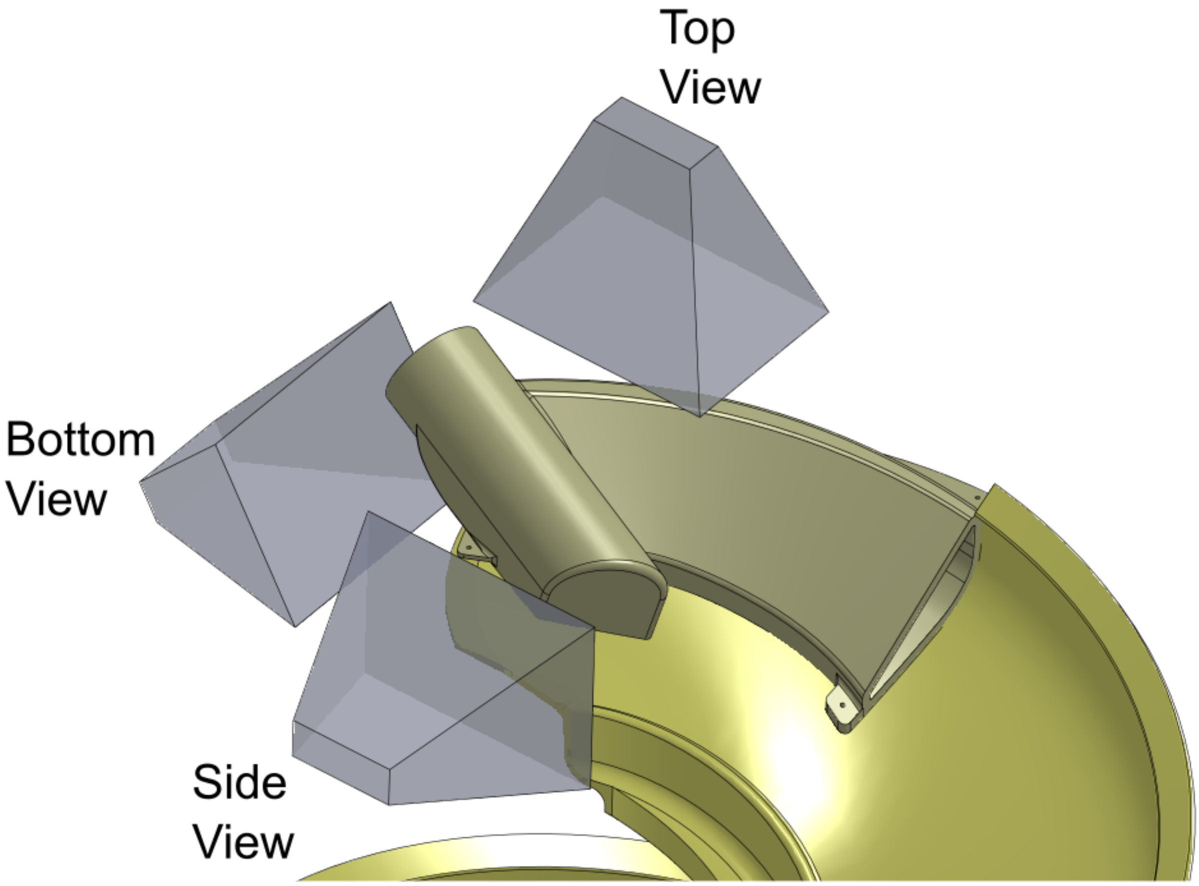

Figure 19: Viewpoints used in Figure 18

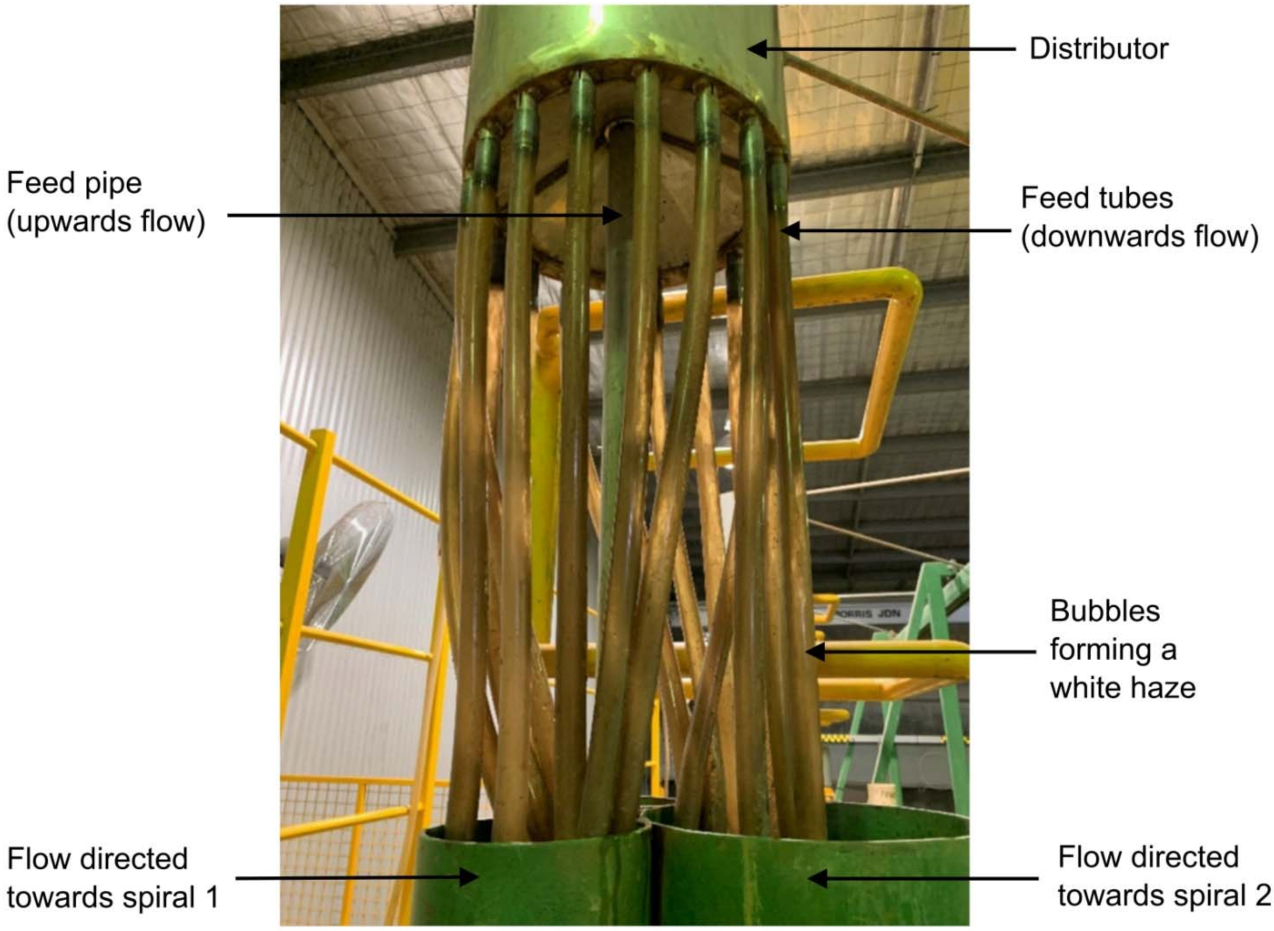

Figure 20: View of the flow through after the distributor showing a large quantity of suspended bubbles as a white haze

As multiple spirals were fed by a single feed source, the inlet flow was split using a so-called ‘distributor’, as indicated in Figure 20, raised high above the spiral’s feed box entry level. The pumped, upwards flow from the feed pipe entered the distributor and created a small water fountain therein to dissipate any pump variability in the flow. The water subsequently settled in the distributor and drained through a series of feed tubes which took the flow down to two spirals, thereby splitting the flow. The translucent nature of the feed tubes shows that many suspended bubbles were present in the downwards flow from the distributor. The bubble’s origin is then likely caused by air being entrained through the fountain-like flow spreading in the distributor.

The suspended bubbled in the spiral’s supply system finding clearly shows that a realistic computational fluid flow analysis should include bubbles entering the fluid domain, using the previously determined bubble size. To the best of the authors’ knowledge, no such bubble phase has been included in fluid analysis efforts so far.

4 Discussion

The porosity of the polyurethane wear layer of the spiral trough has been shown to be an issue in roughness measurements. Although all roughness values show a lower value for the wetted-in compared with the non-wetted-in surface, the large differences in porosity amongst the specimens, evident by a large standard deviation, overshadows possible roughness differences resulting from the wetting-in process. The Maximum Roughness Height (Rz) metric best alleviates this issue, making the wetted-in roughness value of 138.4 μm the most representative roughness value of a spiral trough. Microscopic imaging revealed that the porosity is not limited to the top of the wear layer surface but is also spread through the thickness of the specimen.

A clear distinction between the wetted-in and the non-wetted-in trough surface was found through the wall contact angle measurements. The wetted-in trough surface has a lower wall contact angle of 88.14°, measured in the water phase, compared with that of the non-wetted-in surface. The lower wall contact angle is clear evidence of the removal of the hydrophobic release agent layer on the spiral trough surface through the wetting-in process.

Overall, if a spiral manufacturer aims to reduce or eliminate the wetting-in process during spiral commissioning, which would save time and money for both the spiral manufacturer and the client, the wall contact angle, more so than the surface roughness, should be aimed to be corrected during or after the manufacturing process. Although these experiments were conducted on a CS1 model spiral, the common usage of polyurethane as a wear layer in spirals allows the results to be applied to different spiral models and makes.

Measurements were taken of the water free surface and bubble line position and width using a customised jig at six sampling locations along the spiral trough. The same jig was also utilised to measure the empty spiral trough at the same sampling locations. These free surface measurements can be used directly or, in the case of different spiral makes and models, can be used quantitively to validate a CFD model. Ideally other spiral makes and model could be subjected to the same measurement techniques. Future improvements in 3D scanning could potentially simplify the measurement of the free surface shape.

A novel comparison of the free surface of water-only and two slurry flows was presented which showed that the free surface shape of the slurries coincides with that of the water free surface shape after a certain spiral radius. This showed that particle interaction drives the free surface shape at lower radii whereas the water phase dominates the free surface shape at larger radii. This finding has potential consequences for the forces a moving slurry exerts on the spiral surface, a key parameter in spiral design, as the centripetal forces caused by the moving slurry are likely dominated by the water phase at larger spiral radii. More research efforts are recommended to deepen the understanding of this finding.

It was shown that the start of the water free surface changes rapidly after the feed box but reach a steady state after 1.25 turns down the spiral in the case of the water-only flow. This finding would allow a smaller fluid flow domain in a water-only CFD simulation, which will reduce the required mesh size thus leading to valuable computational savings in such a CFD analysis. Given the ever-changing free surface shape of slurries, no such domain reductions can be recommended when assessing a realistic slurry flow in an existing spiral model. Still, it is expected that the change in the free surface shape due to particle stratification and particle build-up will plateau since particles settled out of the flow or have otherwise found their preferred location. The distance from the feed box to the point of a constant free surface shape would aid in determining the length, referred to commonly as the ‘number of turns’ of a new spiral model and could be a subject of further research.

The bubble line also changes very little after 1.25 spiral turns from the exit of the feed box, both in position and width, for all three fluids. This further supports the case for a shortened fluid flow domain for the CFD simulation of a water-only flow. The position of the bubble line was found to be between 26 and 33 mm below the highest point of the water free surface, which aligns with other researchers’ findings. Although challenging to measure experimentally, the best bubble size estimate, 25 μm, was found by relating the bubbles to the know size of a sampling probe.

Improved methods of bubble size measurement are a research topic worth pursuing. The bubbles were found to be reluctant to coalesce, forming a foam, and were observed to have a small difference in bubble size.

Finally, a translucent feed box showed that the inlet water flow already contains a significant quantity of suspended bubbles. This finding makes the inclusion of a bubble phase, using the estimated bubble size, essential in a fluid analysis of such a spiral flow.

5 Conclusion

This paper has presented an experimental analysis of water-flow and two slurries in a wetted-in, gravity-driven helical mineral separator model that is currently in production to provide an experimental baseline that can be used in the validation of researchers' CFD simulations of spirals. The research conducted herein allowed the following conclusions to be drawn:

- The wall roughness and wall contact angle, two key wall properties not previously measured but essential in any CFD simulation, were measured. The most representative wall roughness metric was found to be the wall roughness height with a value of 138 μm. The wall contact angle of the spiral trough surface was found to be 88.14°, measured in the water phase.
- Novel insights into the wetting-in process were gained as this process was found to affect the wall contact angle to a far greater extent than it affects the surface roughness. A spiral's commissioning costs, incurred by the wetting-in process, can thus be reduced if a correct wall contact angle of the spiral trough is achieved during or after the spiral's manufacturing process.
- The experiments showed that the free surface shape and the position and width of the bubble line in a water-only flow reached a steady state after 1.25 spiral turns, which can significantly improve the efficiency of a water-only flow CFD analysis but is not relevant to slurry flows due to their ever-changing shape.
- As the use of polyurethane for the wear layer is common amongst spiral manufactures, these findings are beneficial to spirals of different makes and models.
- The bubbles that form the often-encountered bubble line are estimated to be 25 μm in

diameter. The bubbles like originate from air entrainment in the distributor and many bubbles were present at the inlet of the feed box. This finding indicates that a realistic computational fluid flow analysis of the flow in mineral separation spirals should include bubbles entering the fluid domain.

Future work will use the observations and measurements presented, and the measured shape of the empty spiral trough surface to inform the modelling choices and settings of a generalised gravity-driven helical mineral separator fluid flow CFD simulation. The free surface and bubble line locations and widths will be used to validate the outcomes of these CFD analysis.

6 Declarations

6.1 Funding

The research study described herein is supported by an Australian Government Research Training Program Scholarship and is co-funded by the Department of Industry, Innovation and Science (Innovative Manufacturing CRC Ltd), the University of Technology Sydney (UTS) and Downer, via its subsidiary Mineral Technologies Pty Ltd (IMCRC/MTC/290418). The funding bodies were not involved in the study design; in the collection, analysis and interpretation of data; in the writing of the report; or in the decision to submit the article for publication.

6.2 Conflicts of interest/Competing interests

Thomas Romeijn is employed by Mineral Technologies whilst being a research student at the University of Technology Sydney (UTS). This research paper reports experimental data on the properties of a CS1 spiral to inform other researchers simulating spiral flows using CFD of essential wall, flow and fluid domain properties. Care has been taken to avoid any value judgement on the mineral separation performance of the CS1 spiral versus other spiral makes and models, thereby avoiding a conflict of interest while enhancing the knowledge of key simulation parameters.

7 Acknowledgment

The research study described herein is supported by an Australian Government Research Training Program Scholarship and is a collaboration between the University of Technology Sydney (UTS), the Innovative Manufacturing Cooperative Research Centre (IMCRC) and Downer, via its subsidiary Mineral Technologies under Grant [IMCRC/MTC/290418]. Thank you to UTS:Rapido, particularly, Hervé Harvard for establishing the research activity. The researchers would like to thank Samuel Gallagher, Myoung Jun Park and Professor Hokyong Shon for their contribution to the findings described in this paper. A special thank-you goes out to David Myint at ATA Scientific for allowing the use of the state-of-the-art tensiometer. The authors appreciate the efforts of David Su in conducting experiments especially his ideas for future avenues of testing. In addition, the many brainstorming sessions with and guidance of Professor David Fletcher are greatly appreciated.

References

[1] Palmer, M.K. and C. Vadeikis. *New developments in spirals and spiral plant operations*. in *XXV International Mineral Processing Congress (IMPC)*. 2010. Brisbane, Australia.

[2] Palmer, M.K. and W.S. Weldon. *A new low cut-point spiral for fine coal separation*. in *Coal Prep International Exhibition and Conference*. 2013. Lexington, USA.

[3] Palmer, M.K. *The Development of a new Low Cut Point Spiral for Fine Coal Processing*. in *XVIII International Coal Preparation Congress*. 2016. Saint-Petersburg, Russia.

[4] Holland-Batt, A.B., *Spiral separation: theory and simulation.* Transactions of the Institute of Mining and Metallurgy (Section C: Mineral Processing and Extractive Metallurgy), 1989. **98**: p. 46-60.

[5] Jain, P.K., *An analytical approach to explain complex flow in spiral concentrator and development of flow equations.* Minerals Engineering, 2021.

[6] Jain, P.K. and V. Rayasam, *An analytical approach to explain the generation of secondary circulation in spiral concentrators.* Powder technology, 2017. **308**: p. 165-177.

[7] Mahran, G.M.A., et al., *CFD Simulation of Particulate Flow in a Spiral Concentrator.* Materials Testing, 2015. **57**: p. 811-816.

[8] Mahran, G.M.A., et al., *Numerical simulation of particulate-flow in spiral separators (15 % solids).* Afinidad, 2015. **72**: p. 223-229.

[9] Doheim, M.A., et al., *Numerical simulation of particulate-flow in spiral separators: Part I. Low solids concentration (0.3% & 3% solids).* Applied Mathematical Modelling, 2013. **37**(1): p. 198-215.

[10] Doheim, M.A., et al., *Computational Prediction of Water-Flow Characteristics in Spiral Separators: Part I, Flow Depth and Turbulence Intensity.* Journal of Engineering Sciences, 2008. **36**: p. 935-950.

[11] Doheim, M.A., et al., *Computational Prediction of Water-Flow Characteristics in Spiral Separators: Part II, The Primary and Secondary Flows.* Journal of Engineering Sciences, 2008. **36**: p. 951-961.

[12] Matthews, B.W., et al., *Computations of curved free surface water flow on spiral concentrators.* Journal of Hydraulic Engineering, 1999. **125**(11): p. 1126-1139.

[13] Wang, J. and J.R.G. Andrews, *Numerical simulations of liquid flow on spiral concentrators.* Minerals Engineering, 1994. **7**(11): p. 1363-1385.

[14] Jancar, T., et al. *Computational and experimental investigation of spiral separator hydrodynamics*. in *Proceedings of the 19th international mineral processing congress: Physical and Chemical Processing*. 1995. San Francisco, USA: Society for Mining, Metallurgy, and Exploration, Inc., Littleton, CO (United States).

[15] Matthews, B.W., C.A.J. Fletcher, and A.C. Partridge, *Computational simulation of fluid and dilute particulate flows on spiral concentrators.* Applied Mathematical Modelling, 1998. **22**(12): p. 965-979.

[16] Matthews, B., et al., *Computational and Experimental Investigation of Spiral Concentrator Flows*, in *Coal 1998: Coal Operators' Conference*, N. Aziz, Editor. 1998: Wollongong, Australia.
[17] Loveday, G.K. and J.J. Cilliers, *Fluid flow modelling on spiral concentrators.* Minerals Engineering, 1994. **7**(2): p. 223-237.
[18] Meng, L., et al., *Effects of cross-sectional geometry on flow characteristics in spiral separators.* Separation Science and Technology, 2021. **56**(17): p. 2967-2977.
[19] Ye, G., et al., *Numerical studies of the effects of design parameters on flow fields in spiral concentrators.* International journal of coal preparation and utilization, 2019: p. 1-15.
[20] Holland-Batt, A.B. and P.N. Holtham, *Particle and fluid motion on spiral separators.* Minerals Engineering, 1991. **4**(3): p. 457-482.
[21] Holtham, P.N., *Particle transport in gravity concentrators and the Bagnold effect.* Minerals Engineering, 1992. **5**(2): p. 205-221.
[22] Holtham, P.N., *Experimental validation of a fundamental model of coal spirals*, in *Australian Coal Association research program (ACARP)*. 1997.
[23] Golab, K.J., P.N. Holtham, and J. Wu. *Validation of a Computer model of fluid flow on the spiral separator*. in *Innovation in Physical Separation Technologies Conference*. 1998. London, UK.
[24] Holtham, P.N., *The fluid flow pattern and particle motion on spiral separators*, in *Faculty of Applied Science*. 1990, Univeristy of New South Wales.
[25] Mineral Technologies. *MT-DS-101 - Data Sheet CS1*. 2014 [cited 20/01/22]; Available from: https://mineraltechnologies.com/images/spirals/MT-DS-101--CS1.pdf.
[26] Holtham, P.N., *Primary and secondary fluid velocities on spiral separators.* Minerals Engineering, 1992. **5**(1): p. 79-91.
[27] Holland-Batt, A.B., *Some design considerations for spiral separators.* Minerals Engineering, 1995. **8**(11): p. 1381-1395.
[28] Wills, B.A. and J. Finch, *Wills' Mineral Processing Technology: An Introduction to the Practical Aspects of Ore Treatment and Mineral Recovery*. 2015: Elsevier Science.
[29] Shakor, P., et al., *Dimensional accuracy, flowability, wettability, and porosity in inkjet 3DP for gypsum and cement mortar materials.* Automation in Construction, 2020. **110**: p. 102964.
[30] AKW Equipment and Process Units. *Spirals AKA-SPIN: for gravity separation of minerals*. 2022 [cited 20/01/22]; Available from: https://www.mining-technology.com/products/spirals-aka-spin/.
[31] Metso:Outotec. *Spiral Concentrator*. 2022 [cited 20/01/22]; Available from: https://www.mogroup.com/portfolio/spiral-concentrator/.
[32] Multotec Group. *Spiral Concentrator*. 2022 [cited 20/01/22]; Available from: https://www.multotec.com/en/spiral-concentrator.